Kua *Biochar (2026)8:33*
https://doi.org/10.1007/s42773-025-00549-w

Biochar

ORIGINAL RESEARCH Open Access

Ascertaining the role of mesopores and macropores in capturing carbon dioxide in multi-hierarchical biochar sorbent: a theoretical and experimental approach

Harn Wei Kua[1*]

Abstract

Biochar is increasingly studied as a potentially carbon-negative material that can also capture and sequester carbon dioxide (CO_2) from air or from a CO_2 stream. Physisorption of CO_2 is identified as the dominant process of CO_2 capture in biochar; it is also widely accepted that micropores play the main role in capturing and storing CO_2 molecules, whereas mesopores and macropores play a secondary role of providing a passageway for CO_2 molecules. This study aims to critically revisit the roles of mesopores and macropores in CO_2 capture. The research objectives include proposing improved mathematical models for calculating fractal dimensions for micropores, mesopores and macrospores in sawdust and biochar samples produced at different temperatures (300 °C, 500 °C, 700 °C, and 1000 °C); the CO_2 capture capability of these sorbents was then correlated with and predicted from their fractal dimensions, pore volume, pore area, pore diameter/width, permeability, and porosity. For mesopores/macropores, the improved fractal dimension model expressed the mercury contact angle on the sorbent pore wall with respect to the surface area covered by mercury. For micropores, the improved model describes the CO_2 adsorption cross-section of the sorbent within the formulation of the Brunauer–Emmett–Teller (BET) theory. It was found that these two models provided more physically realistic values for fractal dimensions (between 2.81 and 3.00) for all the sorbents, compared to existing models. The correlation between CO_2 capture capability and mesopore/macropore permeability ($R^2 = 0.7148$) is lower than the correlations with total pore volume ($R^2 = 0.7894$) and fractal dimension ($R^2 = 0.7433$). Multiple linear regression analyses also showed that only total pore volume and porosity are statistically significant in affecting CO_2 capture by these pores. Scanning electron microscopy revealed "in-foldings" of pore wall in biochar samples produced under high temperature, which can help explain the relatively low correlation between CO_2 captured and pore permeability.

Highlights

- CO_2 capture is correlated with total mesopore/macropore volume ($R^2 = 0.7894$) and fractal dimension ($R^2 = 0.7433$)
- CO_2 capture's correlation with mesopore/macropore permeability is lower ($R^2 = 0.7148$)
- This is due to "in-foldings" on mesopore/macropore pore walls observed in biochar produced at higher temperatures

*Correspondence:
Harn Wei Kua
bdgkuahw@nus.edu.sg

Springer

Keywords Biochar, Carbon capture, Fractal dimension, Mesopores, Macropores, Mercury contact angle

Graphical Abstract

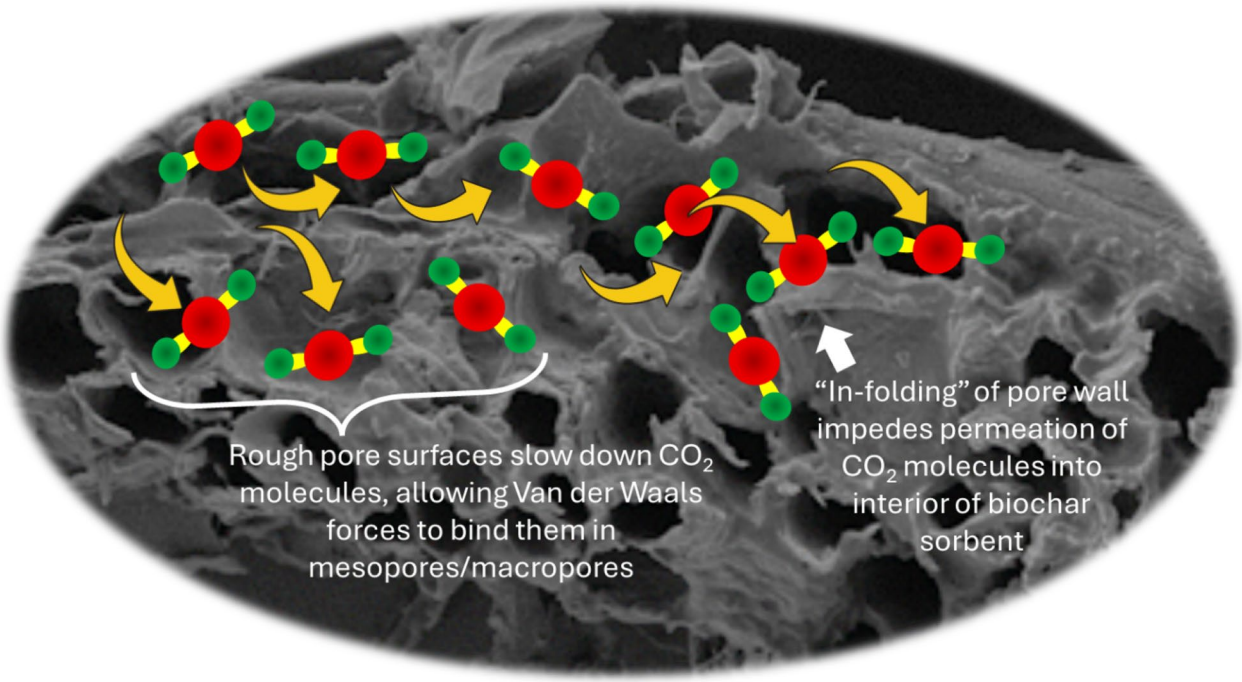

1 Introduction

Biochar has increasingly been studied as a low-cost direct carbon (CO_2) capture sorbent. It is potentially carbon-negative from the life cycle perspective; this can be attributed primarily to the stabilized biogenic carbon (that will otherwise be re-emitted into the atmosphere as CO_2 when the organic feedstock decomposes or is combusted) and the avoided CO_2 emissions resulting from the substitution of fossil fuels by the syngas and bio-oil co-produced with the biochar (Li et al. 2024; Ee et al. 2025). If the produced biochar can also be used to capture CO_2, the additional carbon reduction was estimated to be 4–5% (Dissanayake et al. 2020). Hence, it is important to understand how different properties of biochar affect its CO_2 capture capability.

Although CO_2 capture in biochar occurs through both chemisorption and physisorption, numerous studies have established that CO_2 capture by physisorption on biochar is more dominant than by chemisorption. With respect to physisorption, it has been widely accepted that most of the CO_2 sorption occurs in the micropores, whereas the mesopores and macropores play a secondary and more passive role in directing CO_2 molecules into the micropore network—that is, the mesopores/macropores merely act as a passageway. It is important to verify this notion through a better understanding of how sawdust's and biochar's CO_2 capture capability is related to its myriad physical properties, including surface roughness (which can be described by its fractal dimension). It is hoped that better understanding can provide hints on how these sorbents can be modified, and how this can increase their CO_2 capture capability. However, it is observed that current models for calculating surface fractal dimension may not be applicable to sawdust and biochar, because of the high geometrical complexity of these sorbents. To address this gap in the current literature, the aim of this study is to critically revisit the roles of mesopores and macropores in CO_2 capture.

To achieve this aim, this study has the following research objectives:

- Propose improved mathematical models for calculating fractal dimensions for micropores, mesopores and macrospores of sawdust and biochar samples

produced at different temperatures (that is, 300 °C, 500 °C, 700 °C, and 1000 °C).
- Correlate with, and predict, the CO_2 capture capability of the aforementioned samples with their respective fractal dimensions, pore volume, pore area, pore diameter/width, permeability and porosity.

A review of the state-of-the-art knowledge in chemisorption and physisorption of CO_2 by biochar, and of numerous commonly used mathematical models for calculating fractal dimensions of porous media is important.

For a more complete understanding of how sawdust and biochar can absorb/adsorb CO_2, an understanding of the various types of relevant chemisorption is necessary. The Lewis acid–base interaction between the functional groups on biochar and CO_2 is the most significant chemisorption pathway (Shafawi et al. 2021). Amine (–NH_2) and carboxylic acid (-COOH) can both act as Lewis bases. Remnant alkali and alkaline earth metals (including Ca, Mg, K, and Na) on the biochar can increase its affinity for acidic CO_2 to form carbonates and bicarbonates (Daful et al. 2021; Guo et al. 2022). However, oxygen-containing functional groups can be a double-edged sword for CO_2 capture—although pyrones and ketones of the oxygen-containing functional groups attract CO_2, groups such as carboxylic acids, phenols, lactones, and lactone are acidic, which can also reduce CO_2 chemisorption (Chiang and Juang 2017). Carboxyl (C=O) and hydroxyl (-OH) groups strengthen hydrogen bonding between biochar surfaces and CO_2 molecules with the quadrupole moment (Xing et al. 2014), but surface hydroxyl groups are hydrophilic and attracted water molecules on these adsorption sites can reduce availability for CO_2 capture. Nonetheless, it is generally agreed that biochar with a high C/N content, low O/C content, oxygen content, and high specific surface area is preferred for CO_2 capture (Zhang et al. 2023; Cao et al. 2022).

In physisorption, CO_2 capture capacity is widely believed to rely on micropores less than 1 nm in diameter, because at this size they are close to the dynamic diameter of a CO_2 molecule (Li et al. 2022). Furthermore, the effectiveness of CO_2 sorption by micropore is primarily dependent on the pore structure and specific surface area (Dantas et al. 2021). In contrast, macropores are believed to complement the physisorption role of micropores by enhancing CO_2 diffusion through reducing pressure drop (as the gas passes through the pores), while mesopores provide a passageway for mass transfer at the gas–solid interface (Zhang et al. 2023). In comparing the adsorption performance of potassium hydroxide (KOH)-modified biochar for CO_2 and mercury capture from coal-fired flue gas, Zhang et al. (2025) found that the cumulative surface area of pores smaller than 10 Å has the most influence on CO_2 capture. Di et al. (2025) modified biochar via KOH activation and biomass tar impregnation to improve its CO_2 capture capacity; they found that the effectiveness of CO_2 capture was determined by the predominance of narrow micropores that provided abundant adsorption sites. Their conclusion agrees with those of Alcazar-Ruiz et al. (2024), who found that the reason why KOH activation is the most effective in their study is that the activation process produced the highest volume of micropores (about 0.342 cm^3/g). Using microwave to carbonize the impregnated lignin to increase the micropore structure of biochar, Zhang et al. (2024) verified that CO_2 adsorption on lignin-impregnated biochar was determined mainly by physisorption in micropores, with relatively less influence of chemisorption.

All these conclusions imply that physisorption of CO_2 by a sorbent can be enhanced by adjusting the pore distribution—namely, increasing the volume of micropores and producing small macropores with high specific surface area to produce a multi-hierarchical porous structure (Bari and Jeong 2023).

Understanding physisorption in solids necessitates describing its surface roughness and correlating this quality with different physical properties of the pores in the solid sorbent. Surface characterization by fractal dimension has been increasingly applied to quantitatively describe the heterogeneous and highly disordered pore structure and pore surface roughness of biochar (Wang et al. 2023). Furthermore, efforts have also been made to correlate surface fractal properties of biochar to the various physical and chemical properties, including chemical reactions, distributions of chemical reactivities, and mass transfer of gas in the pore network (Chen et al. 2018; Jia et al. 2024; Hu et al. 2025). Various models have been developed to derive fractal dimension from physical properties of sorbent. For example, using an N_2 adsorption isotherm, the Frenkel–Halsey–Hill (FHH) model (Pomonis and Tsaousi 2009; MacDougall 1947; Halsey 1948; Hill 1952) can be derived:

$$\ln\left(\frac{V}{V_m}\right) = (D-3)ln\left(ln\left(\frac{P_0}{P}\right)\right) + C \tag{1}$$

where V is the adsorbed volume of N_2 at equilibrium vapor pressure, V_m is the volume of the monolayer, P_0 and P are the saturated vapor and equilibrium pressures of N_2 respectively. C is a constant, and D is the fractal dimension of the heterogeneous porous media. Neimark (1990) proposed a thermodynamic approach to deriving the fractal dimension and proposed the following model:

$$\ln S = C - (D-2) ln\, R. \tag{2}$$

where S is the area of the solid–gas interface on the pore, and R is the mean radius of curvature of the pore surface.

The two models above were applied and shown to be appropriate for micropores based on gas adsorption. To describe the wide range of pore sizes in a sorbent, fractal models tailored for mesopores and macropores are also needed for comparison. The model by Zhang and Li (1995) is widely used and its derivation is outlined as follows.

The work done by an applied pressure P to push a certain amount of mercury into pores is equal to the marginal increase in surface energy of the pores in a low energy (nonwetting) situation (Rootare and Prenzlow 1967); that is

$$-PdV = \gamma_L \cos\theta\, dS \tag{3}$$

where γ_L is the surface tension of mercury (N/m^2), θ is the contact angle between the infused mercury and the pore wall, V is the pore volume, and S is the pore surface area. integrating Eq. (3) over all the steps of pressure increments during the MIP experiment, and assuming that θ is constant throughout the experiment, one gets

$$-\int_0^{V_n} PdV \approx -\sum_{i=0}^{V_n} P_i \Delta V_i = \gamma_L \cos\theta \int_0^{S_n} dS = \gamma_L \cos\theta S_n \tag{4}$$

where P_i is the applied equilibrium pressure at each pressure increment in the experiment, ΔV_i is the incremental volume of mercury that infuses into the pores at that particular P_i, and S_n is the corresponding pore surface area covered by the mercury.

Mandelbrot (1983) gave a correlation of the fractal surface area and the volume circumscribed by the surface as

$$S_n^{1/D_{MIP}} \sim V_n^{1/3} \tag{5}$$

where D_{MIP} is the pore surface fractal dimension for the mesopores/macropores calculated from MIP data. Assuming that the fractal area is a Euclidean area Zhang and Li (1995) provided the following scaling relation

$$S_n = k^{D_{MIP}} r_n^2 \left(\frac{V_n^{1/3}}{r_n}\right)^{D_{MIP}} \tag{6}$$

Applying Eq. (6) into Eq. (4), one gets (Zhang and Li 1995)

$$\begin{aligned} &\frac{\sum_{i=0}^{V_n} P_i \Delta V_i}{r_n^2} = k^{D_{MIP}} \gamma_L \cos\theta \left(\frac{V_n^{1/3}}{r_n}\right)^{D_{MIP}} \\ &\Rightarrow ln\left(\frac{\sum_{i=0}^{V_n} P_i \Delta V_i}{r_n^2}\right) = D_{MIP} \cdot ln\left(\frac{V_n^{1/3}}{r_n}\right) + ln\left(k^{D_{MIP}} \gamma_L \cos\theta\right) \end{aligned} \tag{7}$$

This implies that D_{MIP} can be calculated as the gradient of the straight-line graph plotted "$ln\left(\frac{\sum_{i=0}^{V_n} P_i \Delta V_i}{r_n^2}\right)$" against "$ln\left(\frac{V_n^{1/3}}{r_n}\right)$".

Both the FHH's and Niemark's models (Eqs. 1 and 2 respectively) are geometrical in nature. Because they do not consider how the calculated fractal dimensions are related to the surface kinematics of adsorbent (for example, the reaction cross section of the surface) and how it affects gas adsorption, the calculated results are likely to be underestimated. Furthermore, the model created by Zhang and Li (1995), Eq. (7), assumes an average contact angle and this will be inaccurate if the pore surface is highly complex (that is, has high fractal dimension) or when the pore "ink bottle" effect is prominent (this is explained in detail in Sect. 2).

To meet the objectives of this study, a two-stage approach was taken. In the first stage, two improved models for calculating fractal dimensions were proposed. In the first model, fractal dimensions of mesopores/macropores were defined with respect to the pore surface geometry, and data obtained from Mercury Intrusion Porosimetry (MIP) was utilized for validation. In the second model, classical BET theory was used to derive a more comprehensive relation between fractal dimension and surface kinematics of micropores. The calculated fractal dimensions—D_{BET} (for micropores) and D_{MIP} (for mesopores/macrospores)—were then correlated with various physical and chemical properties of teak wood sawdust (used as biochar feedstock) and biochar samples produced at 300 °C (BC300), 500 °C (BC500), 700 °C (BC700) and 1000 °C (BC1000). More details on the methodology are presented in the next section.

2 Materials and methods

2.1 Sawdust feedstock and biochar preparation

Dry sawdust from teak wood was used as biochar feedstock and it was obtained from local carpentry stores. Teak wood was also chosen for earlier works (for example, Gupta et al. 2021; Kua and Tan 2023) because this helps to close the resource loop for wood waste. The raw sawdust was passed through a 200 µm-sieve after visible impurities or debris were removed. The sieved sawdust was then transferred to titanium containers. For BC300, BC500 and BC700, a Nabertherm 1100 °C muffle furnace was used. The heating rate of +10 °C/min was chosen as a slow pyrolysis process; when the residence temperature was reached (for example, for BC300, this was at 300 °C), a residence duration of 1 h was maintained before the biochar sample was cooled down naturally in the furnace (Kua et al. 2025). When the furnace temperature cooled

down to 200 °C, the biochar sample was taken out of the furnace and left to cool in the laboratory environment (at a relative humidity of about 50% and temperature of about 25 °C); this is done to avoid oxidation of the produced biochar (into ash) and thus improve the overall feedstock-to-biochar yield (Kua et al. 2025). To prevent contamination and oxidation, the cooling sample was covered with a metal plate. After the sample was cooled to room temperature, any visible ash was removed from the surface, and only biochar samples that visibly did not contain any ash were collected for analyses; these samples were found at a depth of about 3 cm below the top surface.

For BC1000, a Nabertherm 1300 °C tube furnace was used instead. The sawdust was placed in boat crucibles made from zirconia ($ZrO_2 > 99.5\%$) and calcium oxide ($CaO < 99.9\%$) that were obtained from MTI Corporation Pte Ltd. During heating, three crucibles filled with sawdust were spaced out evenly along the length of the heating tube. The heating rate and cooling procedure were the same as those for the other three types of biochar samples. The residence duration was kept to 15 min to maintain a reasonable feedstock-to-biochar yield (Kua et al. 2025). After heating, biochar samples from these three crucibles were mixed before a sample was extracted for analyses.

2.2 Mercury intrusion porosimetry (MIP)

MIP was conducted using an AutoPore IV 9500 Instrument from Micromeritics Instrument Corporation. Approximately 0.13 g of samples were dried at 60 °C for 12 h and evacuated from the low-pressure port to <50 mmHg to remove the residual gas and moisture. Parameters were evaluated using a contact angle of 130° between the pore surface and mercury. The highest pressure applied in the mercury intrusion process was 59,948.95 psia. With increasing mercury pressure, pore diameters of between 10.11 μm to 3 nm were obtained. A penetrometer volume of 5.9827 mL and mass of 62.8213 g was used. Median pore diameter (volume) was measured at 1.31 psia and 1.559 mL/g, and median pore diameter (area) was measured at 50,547.24 psia and 12.747 m^2/g. This procedure is similar to the one used by Onyekwena et al. (2024).

2.3 Brunauer–Emmett–Teller (BET) measurement with CO_2

BET measurement was done using CO_2 because the aim is to measure specific CO_2-related surface kinematic properties. The use of CO_2 in BET has been shown to be more effective than N_2 for accessing and measuring ultramicropores that may be present in biochar (Kim et al. 2016; Mukhtar et al. 2020). An ASAP2020 Version 4.03 from Micromeritics Instrument Corporation was used. Backfill using nitrogen gas was carried out at the start and end of every analysis run. Sample mass was kept at around 0.3642 g, and CO_2 dosage was performed at a temperature of 22 °C. A low pressure dose of 3.000 cm^3/g STP was applied. A maximum absolute pressure of 769.989624 mmHg was achieved, which corresponded to a relative pressure (P/P_o) of 0.029455247. Analysis based on Density Functional Theory derived a minimum pore width of 0.454 nm.

2.4 Mathematical model development for calculating fractal dimension, D_{MIP}, based on Mercury Intrusion Porosimetry data

As stated above, the model created by Zhang and Li (1995), Eq. (7), assumed that θ is independent of the part of the pore surface area that is covered by the mercury monolayer and that it is sufficiently accurate to represent all values of θ with just an average value. However, this assumption is problematic when the pore surface is highly complex (that is, fractal dimension is high) and/or the "ink bottle" effect is prominent. MIP measures pore size based on the diameter of accessible parts of pores during the intrusion and extrusion cycle. Hence, as shown in Figures S.1(a) and (b), a portion of the intruded mercury is entrapped and so only the diameter of throat pores can be measured, causing the measurement to bias towards small pore sizes. When the mercury droplet flows to the connection between the throat and ink bottle part of the pore (from Figures S.1(c) to (d)), the contact angle can change substantially (that is, from θ_1 to θ_2). Likewise, when a mercury droplet flows into a "bubble projection" (from Figures S.1(e) to (f)), the contact angle can change substantially from θ_3 to θ_4. Therefore, when pore surface and shape complexity increase, θ should be expressed as a function of surface geometry. To consider a high level of surface complexity, the "resolution of analysis" must be increased—that is, we first consider a small area on which the mercury droplet rests and then express θ in terms of this differential area. This expression is applied to Eq. (3) and, finally, we integrate over the entire area covered by the mercury droplet to calculate the total energy required to place the mercury droplet over an area on the sorbent, S_n, when the pressure, P_n, is applied. Because this approach does not involve an average value for θ, it is expected to be more realistic and accurate.

Mathematically, the angle α is defined and treated as a small angle (refer to Figures S.1(e) and (f)), which means that

$$\cos\theta = \sin\alpha \approx \alpha \tag{8}$$

Therefore,

$$\alpha R_{curvature} = y. \tag{9}$$

where $R_{curvature}$ is the average radius of curvature of all the pores that adsorb the mercury. For small α, we assume that the area that is covered by the mercury droplet (S) can be expressed by

$$S = \pi y^2 \Rightarrow y = \sqrt{\frac{S}{\pi}}. \tag{10}$$

Equating Eqs. (9) and (10) yields

$$\alpha = \frac{1}{R_{curvature}}\sqrt{\frac{S}{\pi}}. \tag{11}$$

Applying Eq. (11) to Eq. (4), one gets

$$\begin{aligned} -\sum_{i=0}^{V_n} P_i \Delta V_i &\approx \gamma_L \alpha \int_0^{S_n} dS \\ &= \frac{\gamma_L}{R_{curvature}\sqrt{\pi}} \int_0^{S_n} \sqrt{S} dS = \frac{2\gamma_L}{3R_{curvature}\sqrt{\pi}} S_n^{3/2} \end{aligned} \tag{12}$$

Applying the scaling relation in Eq. (6) to Eq. (12), one gets

$$\begin{aligned} &\frac{\sum_{i=0}^{V_n} P_i \Delta V_i}{r_n^3} = \frac{2k^{3D_{MIP}/2}\gamma_L}{3R_{curvature}\sqrt{\pi}} \left(\frac{V_n^{1/2}}{r_n^{3/2}}\right)^{D_{MIP}} \\ &\Rightarrow ln\left(\frac{\sum_{i=0}^{V_n} P_i \Delta V_i}{r_n^3}\right) = D_{MIP} \cdot ln\left(\frac{V_n^{1/2}}{r_n^{3/2}}\right) + ln\left(\frac{2k^{3D_{MIP}/2}\gamma_L}{3R_{curvature}\sqrt{\pi}}\right) \end{aligned} \tag{13}$$

The values of $P_i \Delta V_i$, r_n and V_n were obtained from the MIP experimental data. Finally, D_{MIP} can be derived from the gradient of the best-fit line graph plotted "$ln\left(\frac{\sum_{i=0}^{V_n} P_i \Delta V_i}{r_n^3}\right)$" against "$ln\left(\frac{V_n^{1/2}}{r_n^{3/2}}\right)$". A schematic summary of the difference between the proposed model and that by Zhang and Li is presented in Fig. 1a. Correlating CO_2 captured with D_{MIP} provides an idea of how surface geometry of mesopores and macropores is related to the adsorption of CO_2 molecules by these pores.

Equation 13 originated from defining θ in terms of S_n. To derive fractal dimensions for micropores (D_{BET}), BET data was used instead and so Eq. (13) is no longer valid; another approach is required.

2.5 Derivation of fractal dimension based on Brunauer–Emmett–Teller (BET) theory, D_{BET}

In this section, a new model for calculating D_{BET} is derived based on the classical BET theory. It is a theory on multilayer physisorption of an adsorbate (CO_2 in our case) by a sorbent (sawdust or biochar), and it has been used to quantify various properties of the sorbent, including specific surface area and total pore volume. It is an extension of the Langmuir theory (a theory for monolayer molecular adsorption) to multilayer adsorption with the assumptions that gas molecules are physically adsorbed in layers infinitely and they only interact with molecules in adjacent layers. The BET theory can be expressed as follows

$$\begin{aligned} &\frac{\frac{P_n}{P_o}}{N_n\left(1-\frac{P_n}{P_o}\right)} = \frac{(c-1)\cdot\left(\frac{P_n}{P_o}\right)+1}{N_m \cdot c} \\ &\Rightarrow N_m = \frac{\left[N_n\left(1-\frac{P_n}{P_o}\right)\right]\cdot\left[(c-1)\cdot\left(\frac{P_n}{P_o}\right)+1\right]}{c\cdot\frac{P_n}{P_o}} \end{aligned} \tag{14}$$

in which n is the index that indicates the step in the increase in applied equilibrium pressure during the BET experiment, P_n is the applied pressure in step n, P_O is the saturation pressure of CO_2 at the adsorption temperature; N_n is the adsorbed gas quantity in step n, whereas N_m is the quantity of gas monolayers adsorbed and c is the *BET constant*. N_m can be related to the total surface area of the pore, S_n, by the BET theory and the scaling relation in Eq. (6),

$$\begin{aligned} &\frac{N_m N_A \sigma_n}{V_{molar.CO_2}} = S_n = k^{D_{BET}} r_n^2 \left(\frac{V_n^{1/3}}{r_n}\right)^{D_{BET}} \\ &\Rightarrow N_m = \frac{V_{molar.CO_2} \cdot k^{D_{BET}} r_n^2}{N_A \sigma_n} \left(\frac{V_n^{1/3}}{r_n}\right)^{D_{BET}} \end{aligned} \tag{15}$$

where N_A is the Avogadro constant, σ_n is the adsorption cross section of sorbent at that particular P_n, $V_{molar.CO_2}$ is the molar volume of CO_2, V_n is the total volume on/in which the CO_2 molecules are adsorbed at the particular P_n, r_n is the pore radius that the adsorbed molecules enable us to measure at the particular P_n, and D_{BET} is the fractal dimension calculated based on BET adsorption data. σ_n, the adsorption cross-section of the sorbent, can also be defined as

$$\sigma_n = \mu_n \frac{M_{molar.CO_2}}{\rho_{sorbent} \cdot N_A} \tag{16}$$

where $\rho_{sorbent}$ is the density of sorbent, and μ_n is the attenuation coefficient of the adsorption process. μ_n can be estimated as a function of the reciprocal of P_n as

$$\mu_n = \frac{\beta_n}{P_n} \tag{17}$$

where β is related to pressure gradient within the multilayer of adsorbed molecules or the change in the equilibrium pressure with the thickness of the multilayer. Equating Eqs. (14) and (15), and substituting σ_n with expressions in Eqs. (16) and (17), one gets

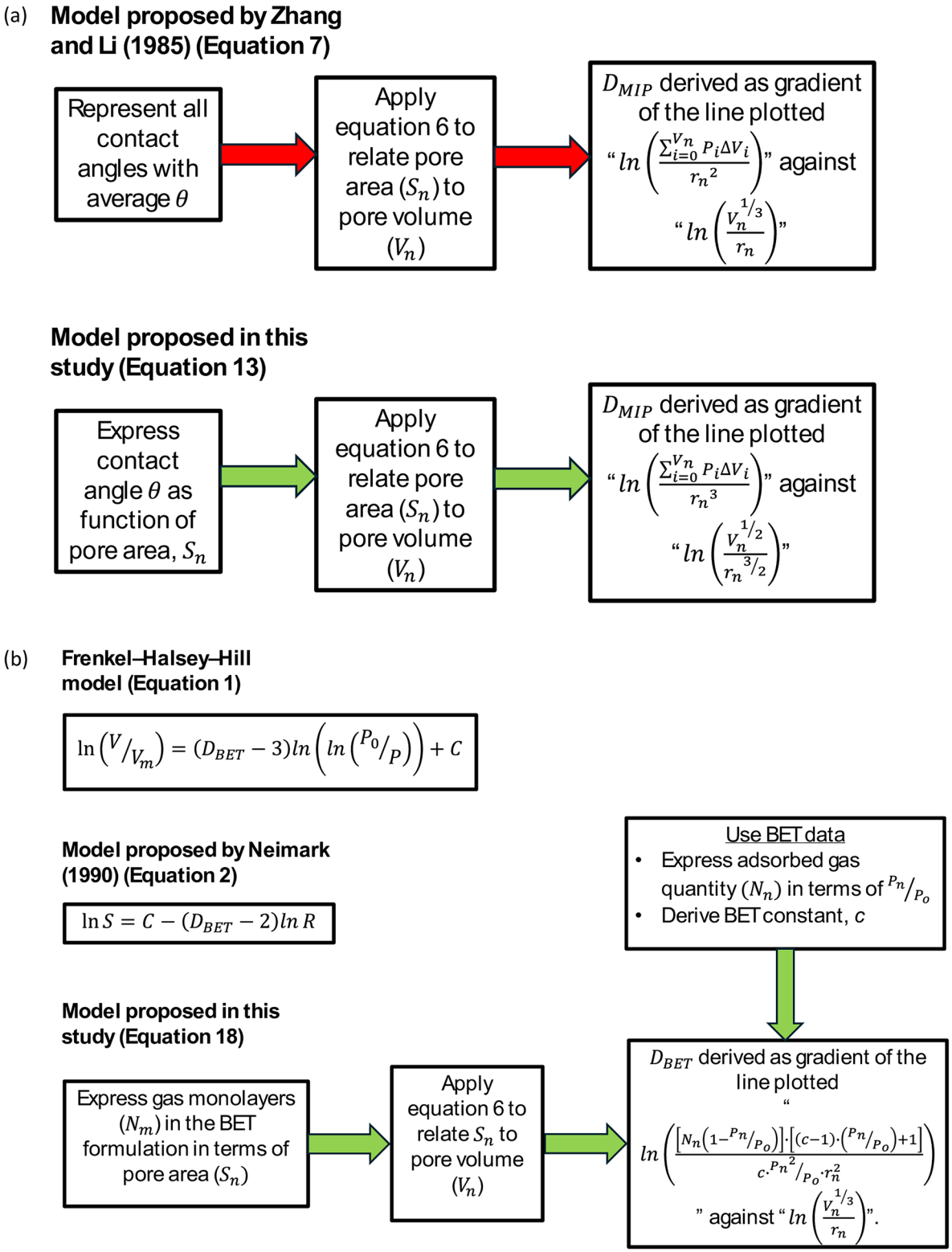

Fig. 1 Comparisons between the two fractal dimension models proposed in this study and established models for **a** mesopores/macrospores, and **b** micropores

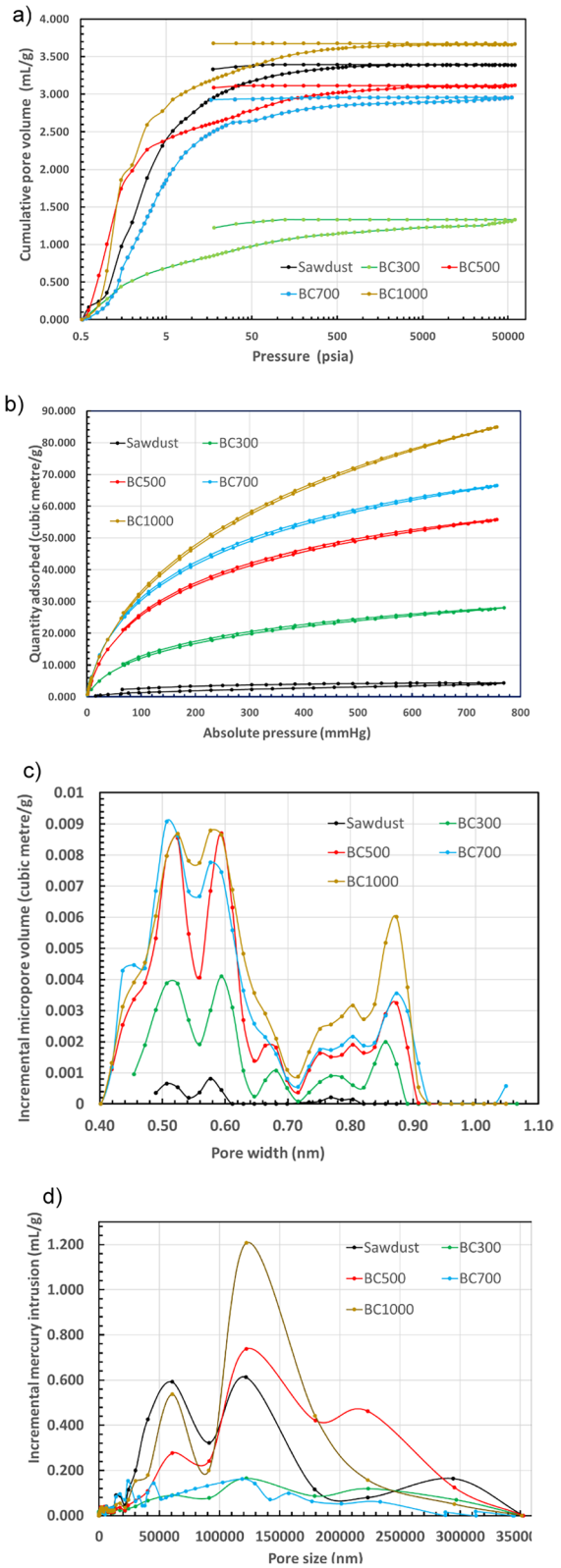

Fig. 2 Pore qualities of sawdust and biochar samples—cumulative volume of adsorption as measured from **a** mercury intrusion and extrusion, **b** CO_2 adsorption and desorption, and distributions of **c** micropores, and **d** mesopores/macropores of sawdust and biochar samples made at 300 °C, 500 °C, 700 °C and 1000 °C

$$\frac{\left[N_n\left(1-\frac{P_n}{P_o}\right)\right]\cdot\left[(c-1)\cdot\left(\frac{P_n}{P_o}\right)+1\right]}{c\cdot\frac{P_n^2}{P_o}\cdot r_n^2}\left(\frac{\beta M_{molar.CO_2}}{\rho V_{molar.CO_2}\cdot k^{D_{BET}}}\right)=\left(\frac{V_n^{1/3}}{r_n}\right)^{D_{BET}}\Rightarrow ln\left(\frac{\left[N_n\left(1-\frac{P_n}{P_o}\right)\right]\cdot\left[(c-1)\cdot\left(\frac{P_n}{P_o}\right)+1\right]}{c\cdot\frac{P_n^2}{P_o}\cdot r_n^2}\right)=D_{BET}\cdot ln\left(\frac{V_n^{1/3}}{r_n}\right)-ln\left(\frac{\beta M_{molar.CO_2}}{\rho V_{molar.CO_2}\cdot k^{D_{BET}}}\right) \tag{18}$$

In Eq. (14), N_n can be expressed in terms of P_n and P_o by using BET experimental data (as shown in Fig. S.2(a, c, e, g and i)). Equation (14) can be rewritten as

$$\frac{\frac{P_n}{P_o}}{N_n\left(1-\frac{P_n}{P_o}\right)}=\frac{(c-1)\cdot\left(\frac{P_n}{P_o}\right)}{N_m\cdot c}+\frac{1}{N_m\cdot c} \tag{19}$$

In the graph plotted "$\frac{\frac{P_n}{P_o}}{N_n\left(1-\frac{P_n}{P_o}\right)}$" versus "$\left(\frac{P_n}{P_o}\right)$", $\left(\frac{c-1}{N_m\cdot c}\right)$ is the gradient and $\left(\frac{1}{N_m\cdot c}\right)$ is the y-intercept. Knowing these two quantities enables us to derive the value of c as follows

$$c=1+\left[\frac{\left(\frac{c-1}{N_m\cdot c}\right)}{\frac{1}{N_m\cdot c}}\right]=1+\frac{Gradient}{y-intercept} \tag{20}$$

Finally, when the value of "c" was found from Eq. (20)—as shown in Fig. S.2(b, d, f, g, and j)—it was substituted into Eq. (18) so that the value of surface pore fractal dimension, D_{BET}, for a certain BET dataset can be calculated from the gradient of the best-fit line graph plotted "$ln\left(\frac{\left[N_n\left(1-\frac{P_n}{P_o}\right)\right]\cdot\left[(c-1)\cdot\left(\frac{P_n}{P_o}\right)+1\right]}{c\cdot\frac{P_n^2}{P_o}\cdot r_n^2}\right)$" against "$ln\left(\frac{V_n^{1/3}}{r_n}\right)$". By correlating CO_2 captured with D_{BET}, we can understand how surface geometry of micropores is related to the adsorption of CO_2 molecules by these pores. A schematic summary comparing the proposed model with the FHH and Neimark's models is presented in Fig. 1b.

3 Results

3.1 Comparisons of D_{MIP} and D_{BET} from different models

MIP measurements indicate that the "ink bottle" effect is prominent in mesopores and macropores (Fig. 2a); this is because the desorption and adsorption parts of the

Table 1 Comparison of calculated fractal dimension based on applying the different theoretical models to BET and MIP data

Sample	D_{BET}			D_{MIP}	
	FHH (Halsey 1948; Hill 1952)	Neimark (1990)	Proposed model	Zhang and Li (1995)	Proposed model
Teak wood sawdust	−0.50 (0.9968)	2.09 (0.7859)	1.84 (0.9903)	3.30 (0.9896)	3.00 (0.9916)
BC300	0.66 (0.9925)	2.17 (0.9254)	1.91 (0.9898)	3.11 (0.9939)	2.81 (0.9946)
BC500	0.26 (0.9779)	2.20 (0.9262)	2.05 (0.9906)	3.18 (0.9854)	2.92 (0.9858)
BC700	1.86 (0.9954)	2.20 (0.9188)	2.06 (0.9983)	3.34 (0.9869)	3.00 (0.9892)
BC1000	1.86 (0.9955)	2.22 (0.9713)	2.06 (0.9986)	3.23 (0.9884)	2.98 (0.9898)

Values in brackets refer to goodness of fit, R^2

isotherms do not coincide (in fact, the desorption parts are almost horizontal). This distinct "ink bottle" effect explains why the model created by Zhang and Li (1995) is inaccurate—it gives $D_{MIP} > 3.00$ (refer to Table 1), which is nonphysical from a surface geometry point of view (Rootare and Prenzlow 1967). In contrast, the model proposed in this work expresses θ with respect to the geometry of the area covered by the mercury monolayer (Figure S.1 in the supporting information, and as derived in Sect. 2) yields $D_{MIP} \leq 3.00$.

On the contrary, Fig. 2b shows much lower "ink bottle" effect in micropores (measured using CO_2 adsorption and desorption). Applying the FHH model to the BET data yields negative D_{BET} values (Table 1). In contrast, the model proposed in this work produces a higher range of goodness-of-fit (R^2) (between 0.9898 (for BC300) and 0.9986 (for BC1000)) than that by Neimark's model (between 0.7859 (for sawdust) and 0.9731 (for BC1000)). This shows that D_{BET} can be derived more accurately by considering reaction kinematics alongside geometrical relation between the average pore radius and pore surface area.

In summary, the results shown in Table 1 show that the models proposed in this study are more suitable than current models for analyzing the sawdust and biochar samples in this study.

3.2 Comparison of pore size distributions

All the four types of biochar samples retain the dominant micropore size of sawdust at about 0.52 nm and 0.58 nm, and the quantities of micropores of these sizes are similar in BC500, BC700 and BC1000 (Fig. 2c). Increasing pyrolysis temperature creates more micropores from 0.7 nm onwards (Fig. 2d). However, the trend is not as clear cut for the mesopores and macropores—BC700 has more pores in the 17.3–100 μm range than the other biochar, while pores of size 100–179.3 μm and 179.3–223.2 μm are dominant in BC1000 and BC500 respectively.

3.3 Correlations among pyrolysis temperatures and pore related properties (including D_{BET} and D_{MIP})

Table 2 shows the various pore related properties measured from both MIP and BET, and the corresponding D_{BET}, D_{MIP} and CO_2 capture capabilities. The increase in pyrolysis temperature increases the values of D_{BET}, total micropore volume and micropore surface area; D_{BET} correlates well with both these properties as well (Fig. 3a, b). However, the correlation between D_{BET} and average pore width is lower ($R^2 = 0.619$: Fig. 3c); this is because the increase in pyrolysis temperature can thermally decompose the biochar walls, while creating more but smaller micropores, instead of increasing the average pore width of existing or new pores.

On the contrary, increasing pyrolysis temperature results in an increase in total mesopore/macropore volume (correlates with D_{MIP}, $R^2 = 0.9316$; Fig. 3d) but a decrease in total mesopore/macropore pore surface area (correlates with D_{MIP}, $R^2 = 0.9862$; Fig. 3e); this can be explained as coalescence of mesopores/macropores. This deduction is supported by the observation that average pore diameter (Fig. 3f) and pore porosity (Fig. 3h) increase with pyrolysis temperature.

When pyrolysis temperature was increased from 300 to 700 °C, even when D_{MIP} increases, a drastic decrease in permeability (to mercury intrusion) is observed at 700 °C and at about $D_{MIP} = 2.92$. Raising pyrolysis temperature from 700 to 1000 °C marginally affects the D_{MIP}, but the permeability increases by 2.5 times (from 19,329.19 mdarcy to 55,218.86 mdarcy, as shown in Table 2). These results (also shown in Fig. 3g) indicate microstructural changes to the mesopores/macropore walls at the higher pyrolysis temperatures.

3.4 Comparisons between CO_2 capture capabilities and pore related properties

Overall, the amount of CO_2 captured increases with pyrolysis temperature—from 1.26 to 3.82 mmol/g of

Table 2 Physical properties of micropores, mesopores and macropores for sawdust and the different types of biochar. CO_2 capture capabilities of all these samples are also shown

Sample	Temperature (°C)	Micropore properties				Mesopore and macropore properties						CO_2 adsorption (cm^3/g of sorbent; BET)	% CO_2 capture (relative to mass of sorbent)	CO_2 captured per unit of sorbent (mmol/g)
		Adsorption average pore width (nm)	Total pore volume (at P/Po = 0.029; cm^3/g)	Total pore area (BET; m^2/g)	D_{BET}	Average pore diameter (nm)	Total volume (mL/g)	Total area (m^2/g)	Porosity (%)	Permeability (mdarcy)	D_{MIP}			
Teak wood sawdust	Not applicable	0.79	0.01	41.18	1.84	2367.77	3.39	5.73	81.55	28,683.64	3.00	4.44	0.88	0.20
BC300	300	1.19	0.05	172.48	1.91	64.66	1.33	82.32	62.82	1172.09	2.81	28.03	5.55	1.26
BC500	500	1.26	0.1	323.7	2.05	489.26	3.12	25.49	77.59	67,873.88	2.92	55.79	11.05	2.51
BC700	700	1.26	0.12	388.16	2.06	8345.29	3.77	1.81	82.33	19,329.19	3.00	66.54	13.17	2.99
BC1000	1000	1.13	0.16	552.91	2.06	1079.16	3.67	13.59	80.98	55,218.86	2.98	84.96	16.82	3.82

sorbent. Although the quantities of micropores are similar in BC500, BC700 and BC1000 (refer to Fig. 2c), the amount of CO_2 captured increases with pyrolysis temperature; this implies that there are other over-riding factors that have larger effect on the amount of CO_2 captured by micropores. In fact, the amount of CO_2 captured is significantly correlated with D_{BET} ($R^2 = 0.9097$; Fig. 4a), total micropore volume ($R^2 = 0.9977$; Fig. 4b) and micropore surface area ($R^2 = 0.9876$; Fig. 4c). On the contrary, the correlation with average micropore width is not as high ($R^2 = 0.8152$; Fig. 4d).

In comparison, CO_2 capture capabilities of mesopores/macropores are less correlated with D_{MIP} ($R^2 = 0.7433$; Fig. 4e), total pore volume ($R^2 = 0.7894$; Fig. 4f), pore area ($R^2 = 0.0756$; Fig. 4g) and pore diameter ($R^2 = 0.3951$; Fig. 4h). The correlation between D_{MIP} and total mesopore/macropore pore area is the lowest, and this phenomenon is consistent with the aforementioned observation that total pore area decreases with pyrolysis temperature (which can be attributed to pore coalescence). Finally, the amount of CO_2 captured by mesopores/macropores has lower correlation with permeability ($R^2 = 0.7148$; Fig. 4i) than with D_{MIP} ($R^2 = 0.7433$; Fig. 4e), pore volume ($R^2 = 0.7894$; Fig. 4f) and porosity ($R^2 = 0.7590$; Fig. 4j). These results provide clear evidence that the sorbents play a more significant role in adsorbing CO_2 into their mesopores/macropores than merely acting as a passageway for these CO_2 molecules. This phenomenon is explained in Sect. 4.3.

3.5 Predicting CO_2 capture from pore properties

While correlations describe how two variables are linked to each other, regression models are used to quantitatively predict the value of a dependent variable based on independent variables.

As shown in Table 3, CO_2 captured by micropores can be accurately predicted by pore width (W_{micro}), pore volume (V_{micro}) and pore area (A_{micro}), at an adjusted $R^2 = 1$. These three variables play a statistically significant role in determining the amount of CO_2 captured, because their p values were 0.015, 0.005 and 0.016 respectively, at the 95% level of confidence. F-statistics is 0.001 (<0.05) and so this model is considered statistically significant and reliable. D_{BET} was not included in this multiple linear regression because it depends on W_{micro}, V_{micro} and A_{micro}; including it will introduce multi-collinearity to the linear model and reduce its overall accuracy.

Similarly, only two independent variables were found to have statistically significant influence on CO_2 captured in the mesopores and macropores (Table 4)—they are the total mesopore/macropore volume ($V_{meso/macro}$; $p = 0.012, < 0.05$) and porosity ($P_{meso/macro}$; $p = 0.013, < 0.05$). Although pore permeability has a reasonably high correlation with the CO_2 captured, its significance was not found to be as high as the aforementioned two variables in this linear model. This is explained in Sect. 4.3.

Finally, the regression relations of micropores (Eq. 21) and mesopores/macropores (Eq. 22) can be summarized as follows:

$$[CO_2]_{micro} = 1.144 W_{micro} + 145.608 V_{micro} - 0.012 A_{micro} - 0.974 \quad (21)$$

$$[CO_2]_{meso/macro} = 44.924 V_{meso/macro} - 5.195 P_{meso/macro} + 272.518 \quad (22)$$

where $[CO_2]_{micro}$ and $[CO_2]_{meso/macro}$ are the percentage of CO_2 captured by the micropores and mesopores/macropores respectively.

4 Discussion

The results above highlighted three unusual relations. Firstly, the increase in pyrolysis temperature leads to an increase in D_{MIP} and pore volume, but a decrease in pore area. This phenomenon was not observed for micropores. Secondly, permeability of mesopores/macropores does not increase monotonically with pyrolysis temperature. Lastly, CO_2 capture by mesopores/macropores is determined by pore volume and porosity, but not permeability. Explanations for these three phenomena are provided in this section.

4.1 Evolutions in pore properties with increase in pyrolysis temperature

Coalescence of pores under heat treatment can be described in terms of the resultant total pore volume using the following relation, assuming that these pores are spherical in shape

(See figure on next page.)

Fig. 3 Correlations between pore fractal dimensions (D_{BET} for micropores and D_{MIP} for mesopores/macropores) and **a** total micropore volume (cm^3/g), **b** total micropore area (m^2/g), **c** average micropore width (nm), **d** total mesopore/macropore volume (mL/g), **e** total mesopore/macropore area (m^2/g), **f** average mesopore/macropore diameter (nm), **g** mesopore/macropore permeability (mdarcy), and **h** mesopore/macropore porosity (%). In each of the graphs, values for the sawdust and four types of biochar (BC300, BC500, BC700 and BC1000) were plotted, and the equations for the best-fit curves were presented

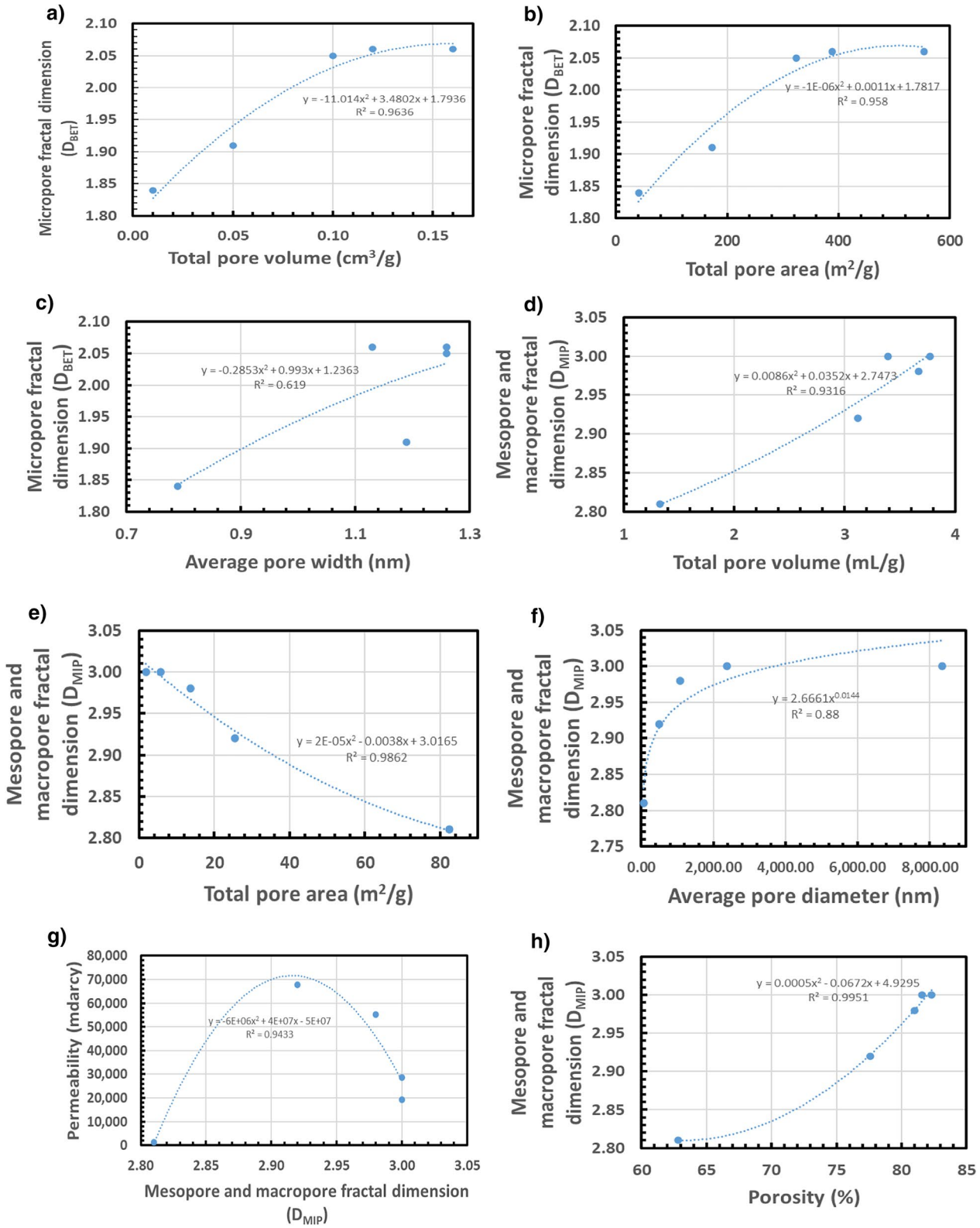

Fig. 3 (See legend on previous page.)

$$R^3 = \sum_{i=1}^{N} \alpha_i r_{old\_i}^3 + \sum_{i=1}^{M} r_{new\_i}^3 - \beta \quad (23)$$

where α_i describes the expansion of old pore i(with size r_{old_i}) as a result of increasing the pyrolysis temperature (for example, from 300 to 500 °C to produce BC500), N represents the maximum number of pores that undergo expansion, M represents the maximum number of newly formed pores at the end of the heating process (in the above example, this particular point in time is when BC500 is created), R is the size of the resultant pore due to the expansion and coagulation of old pores (first term on the right-hand side of Eq. (23)) and the creation and coagulation of new pores of size r_{new_i} (second term on the right-hand side of Eq. (23)), and β accounts for any overlapping of the pores. Equation (23) can be rewritten to derive a general formulation for total surface area of the resultant pore,

$$R^2 = \sum_{i=1}^{N} \left(\frac{\alpha_i r_{old\_i}}{R}\right).r_{old\_i}^2 + \sum_{i=1}^{M} \left(\frac{r_{new\_i}}{R}\right).r_{new\_i}^2 - \frac{\beta}{R} \quad (24)$$

Since $\frac{R}{r_{old\_i}} > \alpha_i$, hence $1 > \frac{\alpha_i r_{old\_i}}{R}$ and the resultant pore area is smaller than the sum of the old pores before expansion and coagulation—that is, $\sum_{i=1}^{N} \left(\frac{\alpha_i r_{old\_i}}{R}\right).r_{old\_i}^2 < \sum_{i=1}^{N} r_{old\_i}^2$.

The phenomenon that total mesopores/macropores area decreases from BC300 to BC700 (Table 2; Fig. 3e)—that is, $R^2 < \sum_{i=1}^{N} r_{old\_i}^2$—is due to the creation and coalescence of new mesopores/macropores (second term on the right-hand side of Eq. (24)) not being a dominant phenomenon. In other words, as pyrolysis temperature increases from 300 to 700 °C, the mesopores and macropores are dominantly produced by the expansion and/or coalescence of older pores (formed at lower temperatures).

On the other hand, the total micropore area monotonically increases with temperature—that is, $R^2 > \sum_{i=1}^{N} r_{old\_i}^2$—which indicates that the creation of new micropores is more dominant as pyrolysis temperatures increases.

4.2 Changes in permeability of mesopores and macropores with pyrolysis temperatures

Applying the theoretical insight from Eq. (24), the microstructural change caused by increasing pyrolysis temperatures is illustrated in Fig. 5, which is supported by observations from scanning electron microscopy (SEM).

In essence, the increase in D_{MIP} is due to the formation of "secondary pores" due to the expansion and coalescing of older pores (formed at lower temperatures); this increases the total pore volume while decreasing the total pore area (as explained in Sect. 4.1). Increased D_{MIP} implies that the surface non-uniformity (roughness) of the original pore wall has increased. When individual pores enlarge, more connections among them will be established, and this leads to an increase in overall porosity and permeability. However, as the pyrolysis temperature reaches 700 °C, flaking of the biochar pore walls can give rise to projections (or "in-foldings") that block the access to neighboring pores, thus decreasing permeability even if the porosity and pore volume increase. When the temperature reaches 1000 °C, these "in-foldings" were either burnt off or disconnected from the supporting pore walls as a result of pore expansion; this results in an overall increase in permeability again—as observed between BC700 and BC1000. This phenomenon was not observed for the sawdust sample.

4.3 Contributions of mesopore/macropore permeability, porosity, pore volumes and D_{MIP} to CO_2 capture

As reflected in Sect. 3.4, mesopore/macropore permeability (Fig. 4i) has less correlation with CO_2 capture than with D_{MIP} (Fig. 4e), total pore volume (Fig. 4f) and porosity (Fig. 4j). How is it possible for these mesopores/macropores to adsorb CO_2 molecules?

CO_2 physisorption is mainly driven by van der Waals forces and pore filling of inflowing CO_2 molecules (Alcazar-Ruiz et al. 2024). Pore filling occurs mainly in micropores, because their size is close to the dynamic diameter of a CO_2 molecule (Li et al. 2022). However, as shown in Fig. 6, when the pore surface is rough—that

(See figure on next page.)

Fig. 4 Correlations between CO_2 capture by sawdust and biochar samples and different pore properties: **a** micropore fractal dimension, **b** total micropore volume (cm^3/g), **c** total micropore area (m^2/g), **d** average micropore width (nm), **e** mesopore/macropore fractal dimension, **f** total mesopore/macropore volume (mL/g), **g** total mesopore/macropore area (m^2/g), **h** average mesopore/macropore diameter (nm), **i** mesopore/macropore permeability (mdarcy) and **j** mesopore/macropore porosity (%). In each of the graphs, values for the sawdust and four types of biochar (BC300, BC500, BC700 and BC1000) were plotted, and the equations for the best-fit curves were presented

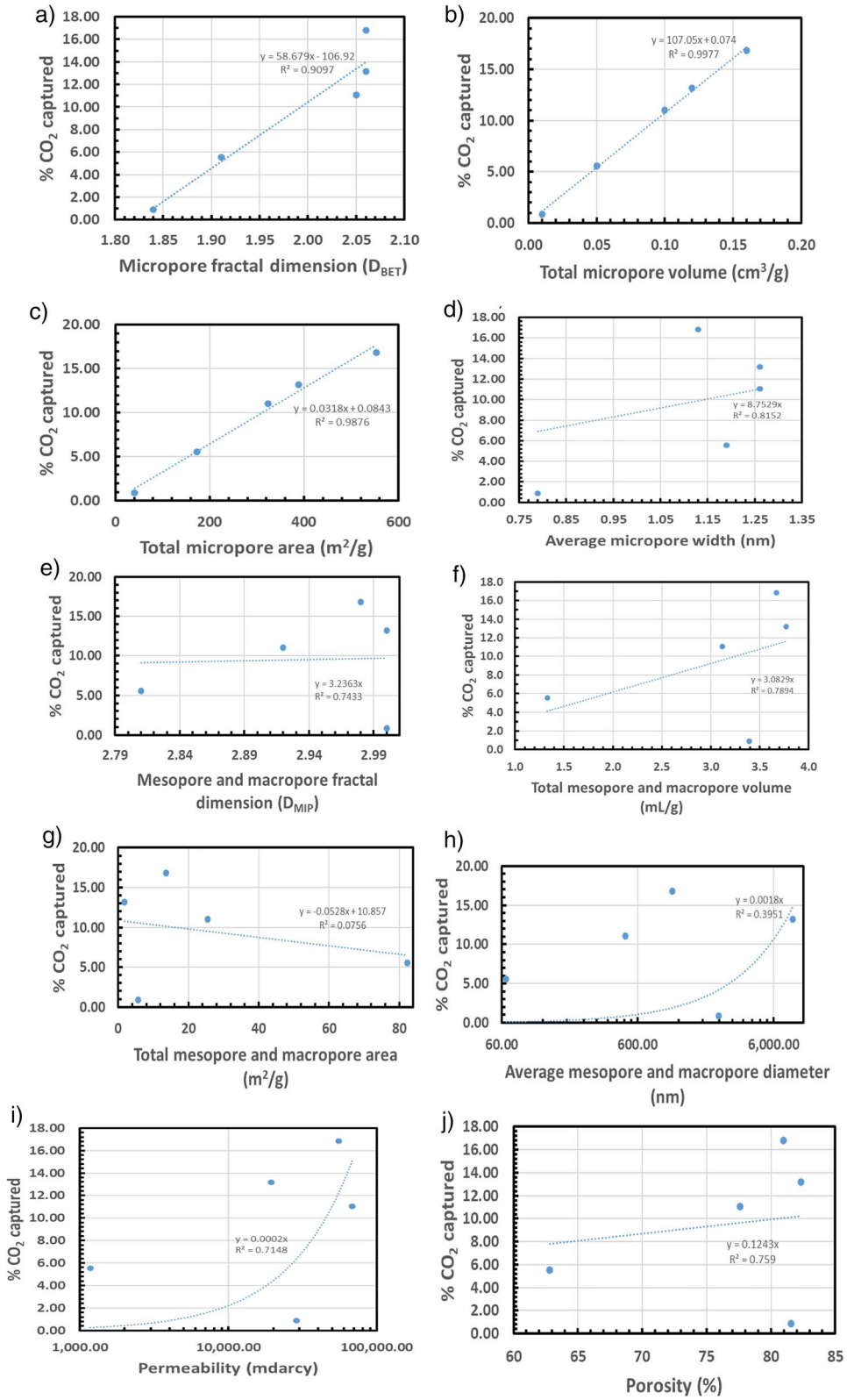

Fig. 4 (See legend on previous page.)

Table 3 Results of multiple linear regression aimed at predicting CO_2 captured by micropores from average micropore width (nm), total micropore volume (cm^3/g) and total micropore area (m^2/g) at 95% level of confidence

Regression statistics (micropores)						
Multiple *R*						1.000
R square						1.000
Adjusted *R* square						1.000
Standard error						0.006
Observations						5.000
ANOVA						
	df	**SS**	**MS**	***F***		**Significance *F***
Regression	3.000	159.417	53.139	1,425,652.871		0.001
Residual	1.000	0.000	0.000			
Total	4.000	159.417				
	Coefficient	**Standard error**	***t* Stat**	***p* value**	**Lower 95%**	**Upper 95%**
Intercept	−0.974	0.027	−36.076	0.018	−1.317	−0.631
Average micropore width (nm)	1.144	0.028	41.078	0.015	0.790	1.498
Total micropore volume (cm^3/g)	145.608	1.099	132.447	0.005	131.639	159.577
Total micropore area (m^2/g)	−0.012	0.000	−38.829	0.016	−0.016	−0.008

Table 4 Results of multiple linear regression aimed at predicting CO_2 captured by mesopores and macropores from total pore volume (mL/g) and porosity (%) at 95% level of confidence

Regression statistics (mesopores and macropores)						
Multiple *R*						0.990
R square						0.979
Adjusted *R* square						0.958
Standard error						1.288
Observations						5.000
ANOVA						
	df	**SS**	**MS**	***F***		**Significance *F***
Regression	2.000	156.096	78.048	47.011		0.021
Residual	2.000	3.320	1.660			
Total	4.000	159.417				
	Coefficient	**Standard error**	***t* Stat**	***p* value**	**Lower 95%**	**Upper 95%**
Intercept	272.518	31.388	8.682	0.013	137.466	407.570
Total volume (mL/g)	44.924	4.900	9.167	0.012	23.839	66.009
Porosity (%)	−5.195	0.599	−8.671	0.013	−7.773	−2.617

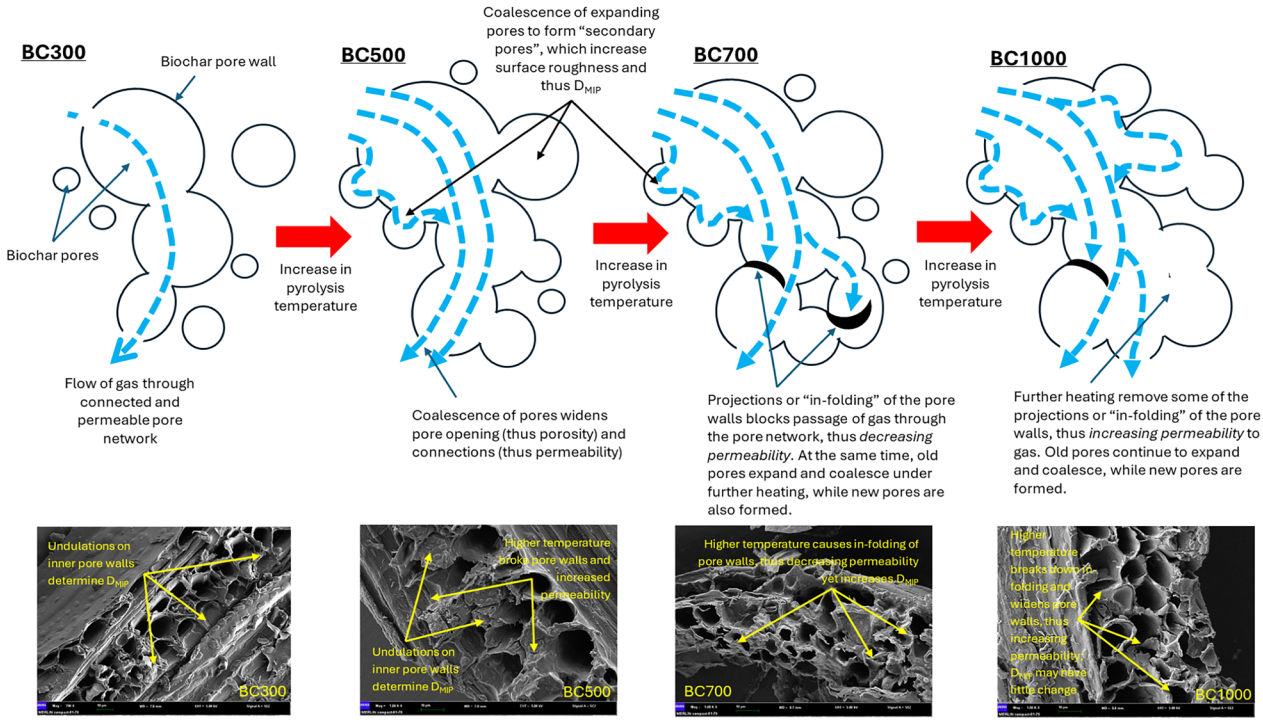

Fig. 5 Graphical model and scanning electron microscope (SEM) images showing the effects of increasing pyrolysis temperature on pore volume, permeability and porosity, due to the expansion and coalescence of old pores and creation of new pores; the effect due to creation and destruction of projections (or, "in-folding") of pore walls on permeability is also explained. Sawdust samples are not shown. The area highlighted in the dotted box is used in Fig. 6 to explain how CO_2 molecules can be adsorbed into the pores due to the highly uneven surfaces (that is, high D_{MIP})

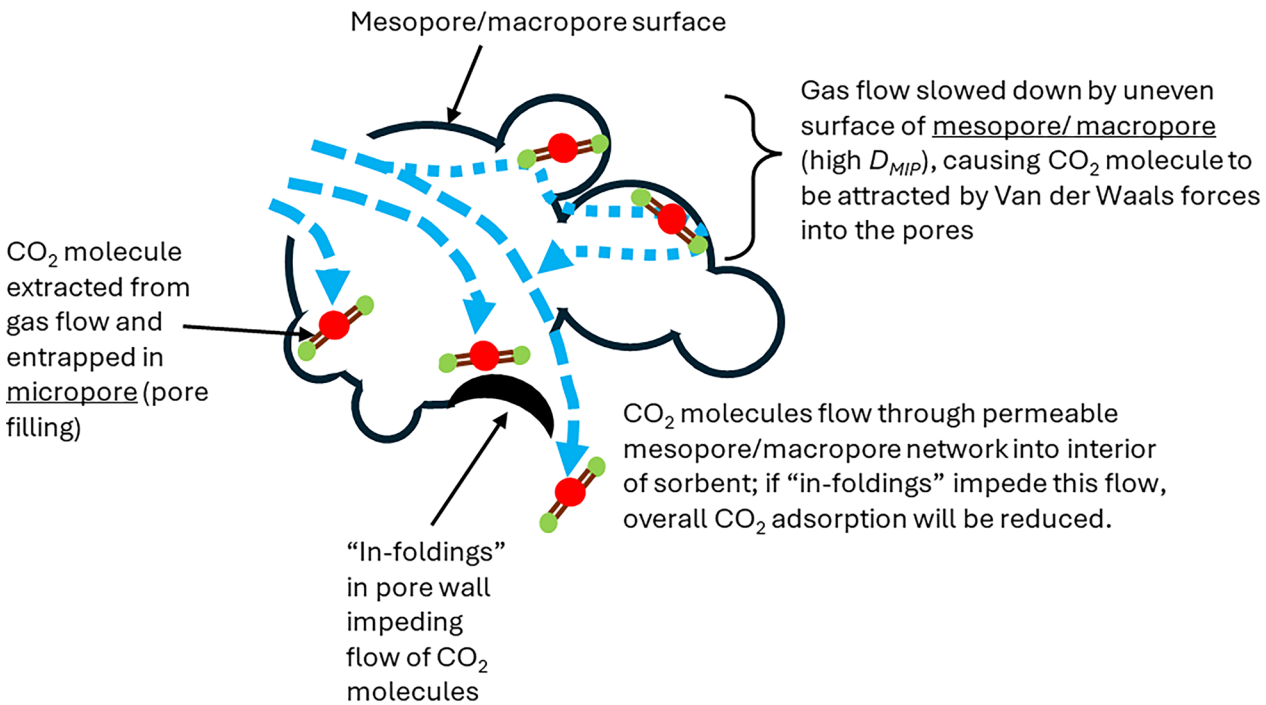

Fig. 6 A possible situation where the mesopore/macropore network is permeable to CO_2 flow and the uneven mesopore/macropore surfaces (high D_{MIP}) promote CO_2 adsorption (for example, attraction by Van der Waals forces) by slowing down the gas flow around the pores

is, D_{MIP} and total pore volume ($R^2 = 0.9316$) values are high—the uneven surfaces of regions around the mesopores and macropores can slow down the flows of CO_2 molecules. D_{MIP} is also highly correlated with porosity ($R^2 = 0.9951$), which implies that slowing down the gas flow enhances attraction of the CO_2 molecules by Van der Waals forces into these pores.

If CO_2 molecules flow into the pore network farther away from the pore surfaces (Fig. 6), they can permeate deeper into the sorbent where they can eventually be adsorbed by other pores (micropores, mesopores and/or macropores). However, this is dependent on whether the CO_2 flow encounters any of the aforementioned "in-foldings" that impede diffusion. Such impedance will reduce the reach of the CO_2 molecules into the sorbent, thus reducing the net amount of CO_2 capture. This is a possible explanation for the relatively low correlation between CO_2 capture and permeability ($R^2 = 0.7148$).

5 Conclusion

This study sets off to improve the derivations of fractal dimensions for micropores, mesopores and macrospores of sawdust and biochar samples, and then verify the roles of mesopores/macropores in capturing CO_2. The key findings can be summarized as follows:

- The D_{BET} and D_{MIP} derived from the models proposed in this study provide better representations of the experimental data. The reasons are that the proposed model for micropores considers the kinematics of adsorption of CO_2 molecules, and the model for mesopores/macropores considers the complex relation between the contact angle of the mercury and geometry of the surface that it covers
- The increase in pyrolysis temperatures increases D_{BET}, total pore volume, pore area and pore radius. CO_2 capture capability is also strongly correlated with all these properties
- The increase in pyrolysis temperatures increases D_{MIP}, total pore volume and pore size, but decreases total pore area; this can be attributed to pore enlargement and coalescence. The increase in pyrolysis temperature does not monotonically increase permeability; this is because complex changes in the microstructures of the mesopores/macropores, such as creation of "in-foldings" of pore walls, can impede gas flows into the sorbent at higher temperatures.
- More importantly, contrary to common knowledge, it is shown that the correlation between CO_2 capture capability and pore permeability is lower than those with total pore volume and D_{MIP}. Henceforth, the role of mesopores and macropores is not restricted to providing a passageway for CO_2 molecules to enter the sorbent.
- Multiple linear regression analyses show that CO_2 capture capability of micropores can be predicted by their average radius, total volume and total area. In contrast, CO_2 capture capability of mesopores/macropores can only be predicted by their total volume and porosity.

One limitation of this study is that chemical functional groups on the sorbent have not been fully analyzed; specifically, how any difference in the amount of C=O, –OH, $–NH_2$ and –COOH on the sorbent can be correlated with changes in D_{BET}, D_{MIP}, and other properties relevant to CO_2 capture should also be studied. Such a study will be essential for us to design low-cost, effective multi-hierarchical porous CO_2 sorbent in the future.

Future research should also examine more consistent methods of increasing D_{MIP} and then correlate it with any changes in CO_2 capture capabilities. These methods may include mechanical means, such as grinding and ball-milling.

Measurements of CO_2 adsorption were carried out at ambient temperature of 22 °C. Another improvement that can be made in future studies is to vary the temperature and pressure at which the different types of biochar samples are dosed with CO_2 and then evaluate the influence of D_{BET} and D_{MIP} on their CO_2 capture capabilities. This is important because biochar may be considered for use as a carbon adsorber under different environmental conditions (including temperature and pressure).

Supplementary Information

The online version contains supplementary material available at https://doi.org/10.1007/s42773-025-00549-w.

Additional file 1.

Author contributions

Harn Wei Kua: Conceptualization; Funding acquisition; Project administration; Supervision; Resources; Data curation; Formal analysis; Investigation; Methodology; Software; Validation; Visualization; Writing—original draft; Writing—review & editing. The author read and approved the final manuscript.

Funding

This work was supported by the College of Design and Engineering Dean's Chair fund (E-471-00-0010-03) and Research Support Fund (E-471-00-0009-02).

Data availability

The author declares that the data supporting the findings of this study are available within the paper and the supplementary information file.

Declarations

Competing interests

Harn Wei Kua is an EBM of the journal Biochar, and he was not involved in the peer-review or handling of the manuscript. The author declares no competing interests.

Author details
[1]Department of the Built Environment, College of Design and Engineering, National University of Singapore, Singapore 117566, Singapore.

Received: 20 June 2025 Revised: 1 November 2025 Accepted: 6 November 2025
Published online: 26 February 2026

References

Alcazar-Ruiz A, Maisano S, Chiodo V, Urbani F, Dorado F, Sanchez-Silva L (2024) Enhancing CO_2 capture performance through activation of olive pomace biochar: a comparative study of physical and chemical methods. Sustain Mater Technol 42:e01177

Bari GAR, Jeong JH (2023) Porous carbon for CO2 capture technology: unveiling fundamentals and innovations. Surfaces 6(3):316–340

Cao L, Zhang X, Xu Y, Xiang W, Wang R, Ding F, Hong P, Gao B (2022) Straw and wood based biochar for CO_2 capture: adsorption performance and governing mechanisms. Sep Purif Technol 287:120592

Chen J, Fang D, Duan F (2018) Pore characteristics and fractal properties of biochar obtained from the pyrolysis of coarse wood in a fluidized-bed reactor. Appl Energy 218:54–65

Chiang YC, Juang RS (2017) Surface modifications of carbonaceous materials for carbon dioxide adsorption: a review. J Taiwan Inst Chem Eng 71:214–234

Daful AG, Chandraratne MR, Loridon M (2021) Recent perspectives in biochar production, characterization and applications. IntechOpen, London

Dantas S, Struckhoff KC, Thommes M, Neimark AV (2021) Pore size characterization of micro-mesoporous carbons using CO2 adsorption. Carbon 173:842–848

Di H, Zhang T, Ma H, Zhang G, Li K, Han J, Yang J (2025) Biomass tar modified biochar with enhanced micropores and oxygen content for high efficiency CO2 capture. Sep Purif Technol. https://doi.org/10.1016/j.seppur.2025.134678

Dissanayake PD, You S, Igalavithana AD, Xia Y, Bhatnagar A, Gupta S, Kua HW, Kim S, Kwon JH, Tsang DC, Ok YS (2020) Biochar-based adsorbents for carbon dioxide capture: a critical review. Renew Sustain Energy Rev 119:109582. https://doi.org/10.1016/j.rser.2019.109582

Ee AWL, Chew SJ, Khoo HH, Ng ATS, Kua HW (2025) Circular economy for the building industry: life cycle assessment of biochar-enhanced concrete. Resour Conserv Recycl 223:108537. https://doi.org/10.1016/j.resconrec.2025.108537

Guo S, Li Y, Wang Y, Wang L, Sun Y, Liu L (2022) Recent advances in biochar-based adsorbents for CO2 capture. Carbon Capture Sci Technol 4:100059. https://doi.org/10.1016/j.ccst.2022.100059

Gupta S, Muthukrishnan S, Kua HW (2021) Comparing influence of inert biochar and silica rich biochar on cement mortar–hydration kinetics and durability under chloride and sulfate environment. Constr Build Mater 268:121142. https://doi.org/10.1016/j.conbuildmat.2020.121142

Halsey G (1948) Physical adsorption on non-uniform surfaces. J Chem Phys 16(10):931–937

Hill TL (1952) Theory of physical adsorption. Advances in catalysis, vol 4. Academic Press, New York, pp 211–258

Hu J, Yang S, Cornelis WM, Huang Q, Qi S, Jiang Z, Qiu H, Xu Y (2025) Biochar amendment mitigates negative effects of controlled irrigation on paddy soil structure: insights from micro-pore network analysis. Agric Water Manag 314:109517. https://doi.org/10.1016/j.agwat.2025.109517

Jia A, Song X, Li S, Liu Z, Liu X, Han Z, Gao H, Gao Q, Zha Y, Liu Y, Wu X (2024) Biochar enhances soil hydrological function by improving the pore structure of saline soil. Agric Water Manag 306:109170

Kim KC, Yoon TU, Bae YS (2016) Applicability of using CO2 adsorption isotherms to determine BET surface areas of microporous materials. Microporous Mesoporous Mater 224:294–301

Kua HW, Tan SMH (2023) Novel typology of accelerated carbonation curing: using dry and pre-soaked biochar to tune carbon capture and mechanical properties of cementitious mortar. Biochar 5(1):36

Kua HW, Goel A, Teo JHJ (2025) Carbon mineralization, microstructure development and mechanical properties of limestone calcined clay cement enhanced with rice husk ash and biochar (bio-LC^3). J Clean Prod 520:146091. https://doi.org/10.1016/j.jclepro.2025.146091

Li Y, Liu L, Yu H, Zhao Y, Dai J, Zhong Y, Pan Z, Yu H (2022) Synergy of developed micropores and electronic structure defects in carbon-doped boron nitride for CO_2 capture. Sci Total Environ 811:151384. https://doi.org/10.1016/j.scitotenv.2021.151384

Li J, Sun W, Lichtfouse E, Maurer C, Liu H (2024) Life cycle assessment of biochar for sustainable agricultural application: a review. Sci Total Environ 951:175448

MacDougall FH (1947) Kinetic theory of liquids. By J. Frenkel. J Phys Colloid Chem 51(4):1032–1033

Mandelbrot BB (1983) The fractal geometry of nature/revised and, enlarged. W.H. Freeman, New York

Mukhtar A, Mellon N, Saqib S, Lee SP, Bustam MA (2020) Extension of BET theory to CO_2 adsorption isotherms for ultra-microporosity of covalent organic polymers. SN Appl Sci 2(7):1232

Neimark AV (1990) Calculating surface fractal dimensions of adsorbents. Adsorpt Sci Technol 7(4):210–219

Onyekwena CC, Li Q, Wang Y, Alvi IH, Hou Y, Ukaomah CF, Hakuzweyezu T (2024) Impacts of biochar and slag on carbon sequestration potential and sustainability assessment of MgO-stabilized marine soils: insights from MIP analysis. Environ Sci Adv 3(11):1564–1577

Pomonis PJ, Tsaousi ET (2009) Frenkel–Halsey–Hill equation, dimensionality of adsorption, and pore anisotropy. Langmuir 25(17):9986–9994

Rootare HM, Prenzlow CF (1967) Surface areas from mercury porosimeter measurements. J Phys Chem 71(8):2733–2736

Shafawi AN, Mohamed AR, Lahijani P, Mohammadi M (2021) Recent advances in developing engineered biochar for CO_2 capture: an insight into the biochar modification approaches. J Environ Chem Eng 9(6):106869. https://doi.org/10.1016/j.jece.2021.106869

Wang S, Zhou S, Pan Z, Elsworth D, Yan D, Wang H, Liu D, Hu Z (2023) Response of pore network fractal dimensions and gas adsorption capacities of shales exposed to supercritical CO_2: implications for CH4 recovery and carbon sequestration. Energy Rep 9:6461–6485

Xing W, Liu C, Zhou Z, Zhou J, Wang G, Zhuo S, Xue Q, Song L, Yan Z (2014) Oxygen-containing functional group-facilitated CO_2 capture by carbide-derived carbons. Nanoscale Res Lett 9:1–8

Zhang B, Li S (1995) Determination of the surface fractal dimension for porous media by mercury porosimetry. Ind Eng Chem Res 34(4):1383–1386

Zhang C, Ji Y, Li C, Zhang Y, Sun S, Xu Y, Jiang L, Wu C (2023) The application of biochar for CO_2 capture: influence of biochar preparation and CO_2 capture reactors. Ind Eng Chem Res 62(42):17168–17181

Zhang X, Xu H, Xiang W, You X, Dai H, Gao B (2024) Lignin-impregnated biochar assisted with microwave irradiation for CO2 capture: adsorption performance and mechanism. Biochar 6(1):22

Zhang T, Xiong Z, Zhao Y, Zhang J (2025) Comparative study on the adsorption performance of CO2 and Hg in flue gas using corn straw and pine biochar modified by KOH. Sep Purif Technol 359:130757. https://doi.org/10.1016/j.seppur.2024.130757